

POLARIMETRIC GUIDED NONLOCAL MEANS COVARIANCE MATRIX ESTIMATION FOR DEFOLIATION MAPPING

Jørgen A. Agersborg[†], Stian Normann Anfinsen[†] and Jane Uhd Jepsen[‡]

[†]UiT The Arctic University of Norway, Department of Physics and technology, Tromsø, Norway

[‡] Norwegian Institute for Nature Research, Tromsø, Norway

1. ABSTRACT

In this study we investigate the potential for using Synthetic Aperture Radar (SAR) data to provide high resolution defoliation and regrowth mapping of trees in the tundra-forest ecotone. Using in situ measurements collected in 2017 we calculated the proportion of both live and defoliated tree crown for 165 $10m \times 10m$ ground plots along six transects. Quad-polarimetric SAR data from RADARSAT-2 was collected from the same area, and the complex multilook polarimetric covariance matrix was calculated using a novel extension of guided nonlocal means speckle filtering. The nonlocal approach allows us to preserve the high spatial resolution of single-look complex data, which is essential for accurate mapping of the sparsely scattered trees in the study area. Using a standard random forest classification algorithm, our filtering results in a 73.8% classification accuracy, higher than traditional speckle filtering methods, and on par with the classification accuracy based on optical data.

2. INTRODUCTION

The tundra-forest ecotone is the boundary between the (low) arctic tundra and the subarctic forest.

A warming climate is expected to lead to encroachment of woody species into the tundra, however this will be counteracted locally by herbivores such as browsing ungulates or defoliating forest pest insects.

Geometrid moth outbreaks cause defoliation and tree mortality, and can lead to rapid state transitions of the tundra-forest ecotone. Defoliating species such as geometrids usually do not kill their host tree outright, but inflict damage that accumulated over several years, and often in combination with other stressors, leads to an increase in tree mortality [1, 2].

The outbreaks affect large areas, but recovery of the crown layer of the birch forest is highly dependent on local factors such as ungulate browsing, soil moisture and quality.

Variations in local site characteristics are therefore important to gain a better understanding, not only of the impact of a single outbreak, but of the nature of the complicated dynamic of the tundra-forest ecotone.

Remote sensing from satellites provides a valuable contribution by being able to monitor the effects of birch moth outbreaks and regrowth after for vast areas. The approach taken in previous work is to detect defoliation based on coarse resolution (pixel resolution $> 200m$) Normalized Difference Vegetation Index (NDVI) products derived from multispectral optical remote sensing images, and correlating this with field work measurements of larvae densities [3]. This follows the convention that defoliation studies often are based on NDVI products. A literature review published in 2017 shows that 82 % of studies mapping defoliation of broadleaved forest caused by insect disturbance used a single spectral index, and most frequently NDVI [2].

In this work, we will consider Synthetic Aperture Radar (SAR) for primarily three reasons. Firstly, polarimetric SAR data are theoretically able to differentiate between scattering mechanisms such as surface, volume, and double bounce. Hence it could be able to accurately separate live tree crowns (volume scattering) from defoliated trees (double bounce scattering). Secondly, remote sensing products from satellite based SAR are near weather-independent. The Norwegian low arctic tundra has a high average cloud cover percentage, which limits observations by optical satellites. And thirdly, it would be interesting to evaluate how SAR performs when it comes to monitor defoliation. While SAR has been used to monitor *deforestation*, none of the studies of broadleaved forest *defoliation* summarized in [2] used SAR.

For remote sensing to contribute to understanding the complicated dynamics of the tundra-forest ecotone, it is imperative that it manages to separate between trees with live and defoliated crown in a setting where trees are sparse and these two classes are interwoven on a very fine scale. This leads to the stringent requirement that we would like to preserve as much of the spatial resolution as possible. This again inspired us to extend the guided nonlocal means (GNLM) speckle filtering algorithm [4] to estimate complex covariance matrices, preserving the spatial resolution of single-look complex data. A random forest classifier was then employed on the filtered covariance matrices to separate live from defoliated ground plots.

3. DATA COLLECTION AND PREPROCESSING

3.1. In situ data

The data are collected close to Polmak, Norway and Nuorgam, Finland in an area of the subarctic birch forest which stretches across the Norwegian-Finnish border.

The effects of a major birch moth outbreak in the early 2000s on the forest is still clearly visible.

The area of interest (AOI) was studied during fieldwork between August 7th and 11th 2017. As part of the fieldwork, 165 points along six transects crossing the Norwegian-Finnish border were examined. The distance between each point was 50m while the distance between each transect was 200m. The vegetation was characterized for a $10\text{m} \times 10\text{m}$ ground plot centred on each transect point. All trees over 2m in the transect point were measured.

Based on the measurements of the crown area, A , and proportion of the crown with (live) leaves, $p \in [0, 1]$, two variables were derived for each ground plot. The sum live crown area divided by the ground plot area gave the Percentage Live Crown (PLC), $\text{PLC} = \sum_{i \in \text{trees in plot}} \frac{p_i A_i}{10\text{m} \times 10\text{m}}$. Similarly, the Percentage Defoliated Crown (PDC) was calculated by replacing p with $1 - p$. A simple classification scheme was then employed where ground plots with PLC greater than five percent were defined as "live", otherwise, if PDC was greater than five percent it was counted as "defoliated". Of the 165 ground plots, 38 were in the "live" class and 57 in the "defoliated" class.

3.2. Remote sensing data

Two fine resolution quad-polarization RADARSAT-2 scenes from July 25th and August 1st 2017 were obtained. The nominal scene size is $25\text{km} \times 25\text{km}$ with a nominal resolution of $5.2\text{m} \times 7.6\text{m}$ (range \times azimuth). Each product was radiometrically calibrated and terrain corrected using the European Space Agency (ESA) Sentinel Application Platform (SNAP) software. The terrain corrected output products had $10.0\text{m} \times 10.0\text{m}$ spatial resolution.

Next, the data were speckle filtered. The noise-like speckle phenomenon is inherent to all SAR data. Its multiplicative nature, means that despeckling is an important step in the generation of SAR products.

A recent development is the GNLM filter, which uses a co-registered optical image to guide the nonlocal speckle filtering [4]. For the optical guide image, a Sentinel-2 image from July 26th 2017 covering the AOI was obtained from the Copernicus data hub. Atmospheric correction was applied to obtain the top of atmosphere reflectance (TOA). Then all spectral bands with 10.0m spatial resolution, namely red, green, blue, and near infrared (NIR), were extracted. For comparison of classification performance, the NDVI was also calculated, $\text{NDVI} = \frac{\text{NIR} - \text{red}}{\text{NIR} + \text{red}}$.

Since we are interested in the different scattering phenomena, we consider the multilook complex covariance matrix, \mathbf{C} . For each pixel, the complex scattering vector can be written as,

$$\mathbf{s} = [S_{HH}, S_{HV}, S_{VV}]^T \in \mathbb{C}^{3 \times 1} \quad (1)$$

where the first subscript indicates the polarization of the transmitted pulse and the second the received polarization (Horizontal or Vertical). Also, we have assumed reciprocity $S_{HV} = S_{VH}$. Given a set of \mathbf{s} vectors, the sample covariance matrix \mathbf{C} can be computed as the sample mean

$$\mathbf{C} = \langle \mathbf{s}\mathbf{s}^H \rangle \quad (2)$$

where the brackets denotes averaging and the superscript H the conjugate transpose operation. In the SNAP software, the speckle filtering step is combined with the estimation of \mathbf{C} , where the different speckle filtering algorithms determine which complex scattering vectors are used in the averaging operation in Eq. (2).

4. POLARIMETRIC GUIDED NONLOCAL MEANS

Nonlocal algorithms are based on splitting the denoising problem into two steps; 1) Finding good predictors and 2) using these predictors in the estimation [5]. While the boxcar algorithm makes the implicit assumption that the closest pixels make the best estimators, nonlocal algorithms uses a similarity criterion to find estimators.

Many different nonlocal algorithms have been used for speckle filtering, and often the similarity criteria are based on patch-wise similarity measures for robustness [5]. A further extension of nonlocal filtering was proposed in [6], where a guide image was used to help select similar pixels for averaging. The guidance image could be the noisy input itself, a pre-filtered version of it, or another image [6]. An example of the former is [7] which used a guided filtering framework to filter the polarimetric covariance matrices, where the guide used was the noisy SAR image itself.

The use of a coregistered optical image to guide the SAR despeckling was first proposed in [8].

An important aspect of the methodology was that the filtered output was the combination of SAR pixels only, to avoid injecting optical image geometry into the SAR scene [8].

Gaetano *et al.* [9] extended the work in [8] to use a nonlocal means framework, except for strongly heterogeneous areas of the SAR scene.

Also [9] extended the previous work to use patch-based filtering. The need to explicitly test for heterogeneous areas was replaced by reliability tests which removes unreliable predictors in a further development [4].

The previous work only deals with single-channel intensity SAR images [8, 9, 4]. The filtering problem could then be formulated as trying to estimate the "clean" intensity image $\hat{\mathbf{X}}$ based on the original noisy intensity data \mathbf{X} , and with

the help of the coregistered optical guide image \mathbf{O} . The filtering is patch-based, where a patch centred on a pixel with index j is defined as $\mathbf{x}(j) = \{\mathbf{X}(j+k), k \in \mathbb{P}\}$, where \mathbb{P} indicates a set of N spatial offsets with respect to j [4].

The filtering is then done for each patch \mathbf{x} centred on pixel j in the input SAR image, by summing weighted patches centred on pixels i , in search area $\Omega(j)$ around j :

$$\hat{\mathbf{x}}(j) = \sum_{i \in \Omega(j)} w(i, j) \mathbf{x}(i) \quad (3)$$

where the size of the search area Ω is determined by a parameter, and the patch size of $\hat{\mathbf{x}}$ and \mathbf{x} are equal and given by \mathbb{P} . Since each pixel is part of multiple patches, the filtering procedure will estimate each pixel multiple times [4].

Note that the optical data do not enter into Eq. (3), which means that only SAR domain pixels are used for determining the filtered SAR image [4]. It is only used to help determine the weights $w(i, j)$ in Eq. (3)

The weight determining how much the filtering of a patch centred on pixel j is influenced by patch centred on pixel i can then be written as:

$$w(i, j) = C e^{-\lambda[\gamma d_{\text{SAR}}(i, j) + (1-\gamma) d_{\text{OPT}}(i, j)]} \quad (4)$$

where C is a normalizing constant, d_{SAR} and d_{OPT} are patch-based dissimilarity measures in the SAR and optical domain respectively, λ is an empirical weight parameter, and $\gamma \in [0, 1]$ balances the emphasis on SAR versus optical dissimilarity.

For the optical domain, [4] used the normalized sum of Euclidean distance

$$d_{\text{OPT}}(i, j) = \frac{1}{BN} \sum_{b=1}^B \sum_{k \in \mathbb{P}} [\mathbf{o}_b(i+k) - \mathbf{o}_b(j+k)]^2 \quad (5)$$

where B is the number of bands in the optical guide and N is the number pixels in each patch determined by the set of spatial offsets \mathbb{P} .

The SAR dissimilarity measure used in [4] was for multiplicative noise in single polarization intensity data. To extend GNLM to PolSAR data, we chose to use a dissimilarity measure that utilized the polarimetric information. Since each pixel in the input SAR image is a complex scattering vector as defined in Eq. (1), a dissimilarity measure between two such vectors can be defined as

$$d_{(\mathbf{s}_i, \mathbf{s}_j)} = \frac{(\mathbf{s}_j - \mathbf{s}_i)^H (\mathbf{s}_j - \mathbf{s}_i)}{\mathbf{s}_j^H \mathbf{s}_j} \quad (6)$$

If we sum this expression we can get a patch-based dissimilarity between the patches centred on pixel position j and pixel position i

$$d_{\text{SAR}}(i, j) = \frac{1}{N} \sum_{k \in \mathbb{P}} \frac{(\mathbf{s}_{j+k} - \mathbf{s}_{i+k})^H (\mathbf{s}_{j+k} - \mathbf{s}_{i+k})}{\mathbf{s}_{j+k}^H \mathbf{s}_{j+k}} \quad (7)$$

where N and \mathbb{P} is defined as before.

By modifying Eq. (3), we can then find the polarimetric guided nonlocal means (PGNLM) estimate for the covariance matrix as:

$$\mathbf{C}(j) = \sum_{i \in \Omega(j)} w(i, j) \mathbf{s}_i \mathbf{s}_i^H \quad (8)$$

Where the weight $w(i, j)$ is defined in Eq. (4), where d_{OPT} is given in Eq. (5), and d_{SAR} in Eq. (7).

Note that while in the single-channel intensity filtering in Eq. (3), each pixel intensity is estimated multiple times as it is a part of multiple patches, the covariance matrix for pixel position j is only estimated once. It is the weighted sum of contributions from pixels where the patch \mathbb{P} centred on that pixel is sufficiently similar to the target patch.

5. RESULTS

For separating ground plots with live tree crown from those with defoliated tree crown, we train a random forest classifier with 200 trees on the filtered covariance matrices. For comparison we obtained the filtered covariance matrices using the boxcar, enhanced Lee, and intensity-driven adaptive-neighbourhood (IDAN) filters in SNAP. Both boxcar and enhanced Lee filters used a 5×5 window, while the adaptive-neighbourhood size for IDAN was 50.

The PGNLM parameters were set in a heuristic manner, following recommendations in [4]. The search area was set to 39×39 pixels, while the size of the patches to be compared were 9×9 . The balancing factor between SAR and optical dissimilarities, γ in Eq. (4) was set to 0.85, while λ was 0.1. Also the measures to discard unreliable predictors used in [4] was employed.

All the polarimetric information is contained in the elements of \mathbf{C} , and we can further simplify the processing by extracting the properties with relevant information: C_{11} , C_{22} , C_{33} , $|C_{13}|$, and $\angle C_{13}$. Here, C_{11} , C_{22} , C_{33} are the intensities in the HH, HV, and VV channels, respectively, and $C_{13} = |C_{13}| e^{j\angle C_{13}}$ is the crosscorrelation between the complex scattering coefficients in the co-polarized channels HH and VV.

In addition, we compare with the classification result on the four-band optical Sentinel-2 subset used as the guide in PGNLM, as well as the NDVI. All data were divided into 3 parts for k-fold cross validation, and the average accuracy is reported. The result is seen in Figure 1.

We see that PGNLM achieves 73.8 % accuracy for 25 July (red bar), 7.4 percentage points better than second best (refined Lee). For the 1 August dataset (blue bar) PGNLM also achieves 73.8 % accuracy, 9.6 percentage points better than second best (IDAN). The optical data (Sentinel-2 25 July), shown in green bars, achieves 74.7 % accuracy. As expected, the NDVI result is significantly lower since it is a combination of two out of the four bands in the optical dataset.

Figure 2, shows the area containing the transects. For the SAR data, C_{11} , C_{22} , C_{33} is shown in the red, green, and

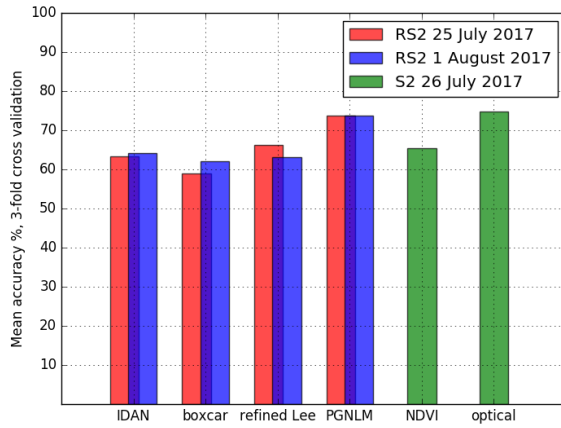


Fig. 1. Random forest classification accuracy.

blue channels respectively. The PGNLM algorithm achieves a significantly smoother result than the other filtering methods, and without any obvious filtering artifacts. This is not unexpected as it averages covariance matrix estimations from a large search area.

6. CONCLUSIONS AND FUTURE WORK

PGNLM filtered SAR data achieve the best accuracy results of the SAR filtering methods, and comparable to optical data. The overall accuracy is not too high, but considering that we try to classify whether one or more trees have leaves in a $10.0\text{m} \times 10.0\text{m}$ area, it might be the best we can hope for. When the ground plots are the same size as the pixel resolution, inaccuracies in geolocation of both satellite and in situ data, as well as the misalignment between sampling grids can be expected to significantly affect the error.

The PGNLM algorithm contains quite a few parameters, that in various ways impact each other. Here they were set in a heuristic manner. For a better understanding, how to set the parameters for polarimetric guided nonlocal means should be explored, as was done for GNLM in [4]. Also, applying PGNLM to standard datasets can help get a more accurate comparison of its performance relative to other polarimetric speckle filtering methods.

7. REFERENCES

- [1] J. U. Jepsen, M. Biuw, R. A. Ims, L. Kapari, T. Schott, O. P. L. Vindstad, and S. B. Hagen, "Ecosystem impacts of a range expanding forest defoliator at the forest-tundra ecotone," *Ecosystems*, vol. 16, no. 4, pp. 561–575, 2013.
- [2] C. Senf, R. Seidl, and P. Hostert, "Remote sensing of forest insect disturbances: current state and future directions," *Int. J. Appl. Earth Observ. Geoinf.*, vol. 60, pp. 49–60, 2017.
- [3] J. U. Jepsen, S. B. Hagen, K. A. Høgda, R. A. Ims, S. R. Karlsen, H. Tømmervik, and N. G. Yoccoz, "Monitoring the spatio-temporal dynamics of geometrid moth outbreaks in birch forest using MODIS-NDVI data," *Remote Sens. Environ.*, vol. 113, no. 9, pp. 1939–1947, 2009.
- [4] S. Vitale, D. Cozzolino, G. Scarpa, L. Verdoliva, and G. Poggi, "Guided patchwise nonlocal SAR despeckling," *IEEE Trans. Geosci. Remote Sens.*, vol. 57, no. 9, pp. 6484–6498, 2019.
- [5] C.-A. Deledalle, L. Denis, G. Poggi, F. Tupin, and L. Verdoliva, "Exploiting patch similarity for SAR image processing: the non-local paradigm," *IEEE Signal Process. Mag.*, vol. 31, no. 4, pp. 69–78, 2014.
- [6] K. He, J. Sun, and X. Tang, "Guided image filtering," *IEEE Trans. Pattern Anal. Mach. Intell.*, vol. 35, no. 6, pp. 1397–1409, 2012.
- [7] X. Ma, P. Wu, and H. Shen, "A nonlinear guided filter for polarimetric SAR image despeckling," *IEEE Trans. Geosci. Remote Sens.*, vol. 57, no. 4, pp. 1918–1927, 2018.
- [8] L. Verdoliva, R. Gaetano, G. Ruello, and G. Poggi, "Optical-driven nonlocal SAR despeckling," *IEEE Geosci. Remote Sens. Lett.*, vol. 12, no. 2, pp. 314–318, 2014.
- [9] R. Gaetano, D. Cozzolino, L. D'Amiano, L. Verdoliva, and G. Poggi, "Fusion of SAR-optical data for land cover monitoring," in *Proc. IEEE Int. Geosci. Remote Sens. Symp. (IGARSS)*. IEEE, 2017, pp. 5470–5473.

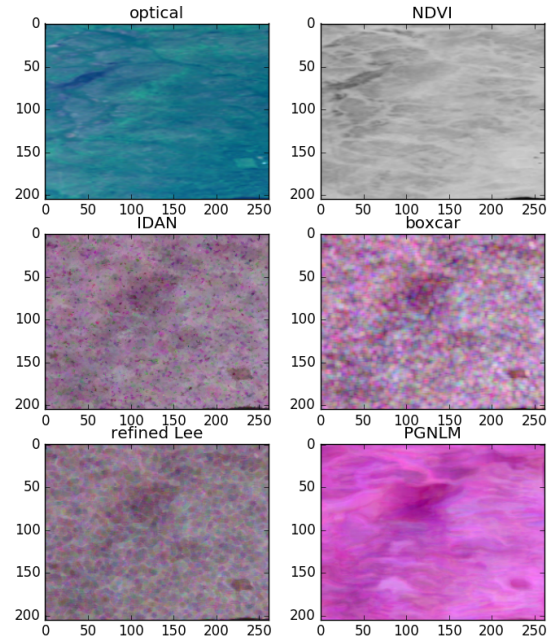


Fig. 2. Filtered SAR data (25 July) and optical data (26 July)